Precise manipulation of iron spin states in single-atom catalytic membranes for singlet oxygen selective production

Na Lu[1,2], Yanle Li[4], Jianqiang Wang[1,2], Guiliang Li[1,2], Guowei Li[2,3], Fu Liu[1,2*], Chuyang Y. Tang[5]

[1] Zhejiang International Joint Laboratory of Advanced Membrane Materials & Processes, Ningbo Institute of Materials Technology & Engineering, Chinese Academy of Sciences, No. 1219 Zhongguan West Rd, Ningbo 315201, China

[2] Ningbo College of Materials Technology & Engineering, University of Chinese Academy of Sciences, 19 A Yuquan Rd, Shijingshan District, Beijing 100049, China

[3] CAS Key Laboratory of Magnetic Materials and Devices/Zhejiang Province Key, Laboratory of Magnetic Materials and Application Technology, Ningbo Institute of Materials Technology & Engineering, Chinese Academy of Sciences, No. 1219 Zhongguan West Rd, Ningbo 315201, China

[4] Yangtze Delta Region Institute (Huzhou), University of Electronic Science and Technology of China, Huzhou, Zhejiang 313000, P. R. China

[5] Department of Civil Engineering, The University of Hong Kong, Pokfulam, Hong Kong, 999077, China

*Corresponding author. E-mail: fu.liu@nimte.ac.cn

Table of Contents

Experimental Procedures

Text S1. Synthesis of Fe-CNs, Co-CNs, Ni-CNs, Mn-CNs, and 4-Fe-CN catalytic membrane (4-Fe-CN-CM)

Synthesis of Fe-CNs: Melamine (MA, 1.513 g) and cyanuric acid (CA, 1.239 g) were dissolved in 320 mL and 256 mL DI water with stirring at 85 ^{o}C for 1 h, respectively. $Fe(NO_3)_3 \bigstar 9H_2O$ (0.323 g) and oxalic acid dihydrate (OA, 0.303 g) were added in 224 mL DI water for dissolution at room temperature for 10 min vigorous stirring, and then this solution was mixed with the CA solution. Following 5 min stirring, the mixed solution was added into the MA solution with continues stirring for 4 h at room temperature. The catalyst precursor was collected by vacuum filtration and dried at 60 ^{o}C overnight, which were then heated to 600 ^{o}C with the heating rate of 2 ^{o}C min^{-1}, 3 ^{o}C min^{-1}, or 4 ^{o}C min^{-1} under flowing Ar atmosphere, and the catalysts were referred as 2-Fe-CN, 3-Fe-CN, and 4-Fe-CN, respectively.

Synthesis of Co-CNs and Ni-CNs: MA (1.513 g) and CA (1.239 g) were dissolved in 320 mL and 256 mL DI water with stirring at 85 ^{o}C for 1 h, respectively. Cobalt acetate (0.0498 g) (or nickel acetate tetrahydrate (0.0499 g))and citric acid (0.127 g) were dissolved in 224 mL DI water at room temperature for 10 min vigorous stirring, and then this solution was added into the CA solution. Following 5 min stirring, the mixed solution was added into the MA solution with continues stirring for 4 h at room temperature. The catalyst precursor was collected by vacuum filtration and dried at 60 ^{o}C overnight, which were then heated to 600 ^{o}C in a tube furnace at a heating rate of 2 ^{o}C min^{-1}, 3 ^{o}C min^{-1}, 4 ^{o}C min^{-1}n under flowing Ar atmosphere, and the catalysts were referred as 2-Co-CN (or 2-Ni-CN), 3-Co-CN (or 3-Ni-CN), and 4-Co-CN (or 4-Ni-CN), respectively.

Synthesis of Mn-CNs: MA (1.513 g) and CA (1.239 g) were dissolved in 320 mL and 256 mL DI water with stirring at 85 ^{o}C for 1 h, respectively. Manganese tris(4-oxopent-2-en-2-oate) (0.0704 g) and citric acid (0.127 g) were dissolved in 224 mL DI water at at 85 ^{o}C for 40 min vigorous stirring, and then this solution was added into the CA solution. Following 5 min stirring, the mixed solution was added into the MA solution with continues stirring for 4 h at room temperature. The catalyst precursor was collected by vacuum filtration and dried at 60 ^{o}C overnight, which were then heated to 600 ^{o}C in a tube furnace at a heating rate of 2 ^{o}C min^{-1}, 3 ^{o}C min^{-1}, 4 ^{o}C min^{-1}n under flowing Ar atmosphere, and the catalysts were referred as 2-Mn-CN, 3-Mn-CN, and 4-Mn-CN, respectively.

4-Fe-CN ethanol solution (0.1 g L^{-1}) was heated (80 ^{o}C) and stirred for 60 minutes followed by ultrasonication for 30 minutes to make homogeneous dispersion. Using vacuum-filtered method through a Nylon membrane to fabricate 4-Fe-CN-CM.

Text S2. Chemicals and characterizations

Chemicals: Melamine (MA, 99%), cyanuric acid (CA, 98%), oxalic acid dihydrate (OA, ≥95%), citric acid monohydrate ($C_6H_8O_7$•H_2O, AR), iron nitrate nonahydrate (FeN_3O_9•$9H_2O$, AR), manganese acetylacetonate ($MnC_{15}H_{21}O_6$), tetracycline (TC, 98%), potassium monopersulfate triple salt (PMS, $KHSO_5$•$0.5KHSO_4$•$0.5K_2SO_4$, ≥47% $KHSO_5$ basis), nitro blue tetrazolium (NBT, 98%), p-terephthalic acid (PTA, 99%), p-benzoquinone (BQ, 99%), hydroxybenzoic acid (HBA, 99%), tert-butyl alcohol (TBA, > 99.5% (GC)), furfuryl alcohol (FFA, AR, 98%,), NaCl, and sodium sulfate anhydrous (Na_2SO_4, AR, 99%) were offered by Aladdin (Shanghai, China). Methyl phenyl sulfoxide (PMSO, 98%), and methyl phenyl sulfone ($PMSO_2$, 98%) were supplied by Macklin (Shanghai, China). Nickel acetate tetrahydrate ($Ni(CH_3COO)_2$•$4H_2O$, Ni>23%, 99%), and cobalt acetate tetrahydrate ($(CH_3COO)_2Co$•$4H_2O$, 98%) were purchased from Energy Chemical (Anhui, China).

Characterizations: The composition of the catalysts was determined by the infrared spectroscopy (FTIR, Thermo, Nicolet 6700, America). The crystal structures were recorded using X-ray diffraction (XRD, Bruker, D8 Advance Davinci, Germany), and the scanning speed was 2.5 ^{o}C min^{-1}. The morphologies of the catalysts and the catalytic membranes were researched via scanning electron microscopy (SEM, Hitachi, S-4800, Japan) and transmission electron microscopy (TEM, ThemoFisher, Talos F200x, America). The atomic-scale distribution images of the catalysts were collected by high-angle annular dark field scanning TEM (HAADF-STEM, ThermoFisher, Spectra 300, America). The thicknesses of the catalyst sheets were measured using atomic force microscope (AFM, Vecco, Dimension 3100, America). The chemical constitution was revealed by the X-ray photoelectron spectroscopy (XPS, Kratos, Axis Ultra DLD, Britain). The ROSs were detected by electron-spin paramagnetic resonance (EPR, Bruker, EMXnano, Germany). The concentration of PMSO, $PMSO_2$, HBA, and BQ were measured by a high performance liquid chromatograph (HPLC, U3000, Dionex, US). X-ray absorption near-edge structure (XANES) spectra and extended X-ray

absorption fine structure (EXAFS) spectra were collected on the BL11B baemline in the SSRF at Shanghai, China. The effective magnetic moments were measured by the superconducting QUantum interference device (SQUID-VSM, America).

Text S3. The EXAFS Signals Fitting and Wavelet Transform (WT) Analysis

The obtained XAFS data was processed in Athena (version 0.9.26) for background, pre-edge line and post-edge line calibrations. Then Fourier transformed fitting was carried out in Artemis (version 0.9.26) [2, 3]. The k^3 weighting, k-range of ~3.0-~10.0 $Å^{-1}$ and R range of ~1.0-~2.5 Å were used for the fitting. The models of Fe foil, FeO, Fe_2O_3, and Fe-CN were used to calculate the simulated scattering paths. The four parameters, coordination number, bond length, Debye-Waller factor and E_0 shift (CN, R, σ^2, ΔE_0) were fitted. For Wavelet Transform analysis, the $\chi(k)$ exported from Athena was imported into the Hama Fortran code [4]. The parameters were listed as follow: R range, 0-3 Å, k range, 3-13.9 $Å^{-1}$; k weight, 3; and Morlet function with $\kappa=5$, $\sigma=1$ was used as the mother wavelet to provide the overall distribution.

Text S4. UV and Liquid Chromatography Spectrometry Methods

TC solution was evaluated by UV-vis spectroscopy [5-8], and the concentration was detected by the absorbance value at 356 nm. Rhodamine B solution was evaluated by UV-vis spectroscopy, and the concentration was detected by the absorbance value at 552 nm.We adopted the standard procedure as follows: (1) preheating the instrument for 30 minutes, (2) all solvents were deionized water, (3) dark correction and solvent correction were performed before the tests, (4) keeping the slit width of the instrument constant. Therefore, the influence of temperature, solvent and slit width on the test results is basically excluded. At the same time, we determined the standard curve of TC (Figure S12).

The concentrations of contaminants (chlorobenzene, SMX, BPA, BQ, HBA, PMSO, and $PMSO_2$) were monitored by a high-pressure liquid chromatographer (HPLC) with a TC-C18 reverse-phase column. To determine the concentration of HBA and BQ, the eluent was the combination of acetonitrile and ultrapure water (30:70) at 1.0 mL/min and the UV detector was set at λ=244 nm. To determine the concentration of PMSO and $PMSO_2$, the eluent was the combination of acetonitrile and 0.1 % H_3PO_4 solutionu (20:80) at 1.0 mL/min and the UV detector was set atλ=230 nm. To determine the

concentration of chlorobenzene, the eluent was the combination of methanol and ultrapure water (70:30) at 1.0 mL/min and the UV detector was set at λ=210 nm. To determine the concentration of SMX, the eluent was the combination of methanol and ultrapure water (30:70) at 1.0 mL/min and the UV detector was set at λ=260 nm. To determine the concentration of BPA, the eluent was the mixture of methanol and ultrapure water (70/30, v/v %) at 1.0 mL/min and the UV detector was set at λ=280 nm.

Text S5. Electrochemical Measurement

Electrochemical measurements were performed in a three-electrode cell, comprising a catalyst-coated fluorine-tin oxide (FTO) glass electrode as the working electrode, an Ag/AgCl as the referrence electrode, a platinum wire as the counter electrode. 1 mg Fe-CNs was mixed with 0.1 mL ethanol to make s slurry. The slurry was then dispersed onto a 2 cm✕1 cm FTO glass and then dried naturally at room temperature. All potentials reported in our work were referenced to a reversible hydrogen electrode (RHE). The linear sweep voltammetry (LSV) experiments were measured in a 0.5 M Na_2SO_4 solution between 0 and -1.0 V vs RHE at a scan rate of 5 mV s^{-1}.

Text S6. DFT Calculations

The spin-polarized density functional theory (DFT) simulations were conducted with the Vienna ab-initio simulation package (VASP) software. [9] The generalized gradient approximation (GGA)-Perdew-Burke-Ernzerhof (PBE) functional was used to compute the exchange-correlation term, [10] and the projector-augmented wave method was applied to calculate the ion-electron interaction. [11] The cut-off energy for the plane-wave-basis set was set as 450 eV, and the energy and force convergence criteria were set as 10^{-4} eV and 0.03 eV/Å, respectively. A 2 × 2 × 1 supercell of g-C_3N_4 unit cells was adopted, and the Brillouin region was sampled with a 2 × 2 × 1 k-point. Å vacuum space in z direction was spplied to avoid the interaction between neighboring images. The dispersion correction was considered with the DFT-D3 correction method of Grimme et al. [12]

Text S7. Equations

We determined the contribution from •OH, $SO_4^{\bullet-}$, $O_2^{\bullet-}$, Fe(IV), and $^1O_2$ quantitively. The quantitation of $O_2^{\bullet-}$ was examined by the NBT method.[14] The Fe(IV) was identified by $PMSO_2$ originate from Fe(IV)-derived PMSO.[15] The reaction rate constants after adding TBA, and MeOH were denoted as k_1, k_2, k_3, and k_4, respectively, and the initial rate constant without quenching agent was k_0. The contributions of •OH, $SO_4^{\bullet-}$, $O_2^{\bullet-}$, Fe(IV), and $^1O_2$ were calculated according to Equations S1-3,[1] respectively.

$$\lambda\ (\bullet OH) = [(k_0 - k_1) / k_0] \times 100\% \quad (1)$$

$$\lambda\ (SO_4^{\bullet-}) = [(k_1 - k_2) / k_0] \times 100\% \quad (2)$$

$$\lambda\ (^1O_2) = 1 - \lambda\ (\bullet OH) - \lambda\ (SO_4^{\bullet-}) - \lambda\ (O_2^{\bullet-}) - \lambda\ (Fe(IV)) \quad (3)$$

where λ (•OH), λ ($SO_4^{\bullet-}$), λ ($O_2^{\bullet-}$) , λ (Fe(IV) and λ ($^1O_2$) were the contribution of •OH, $SO_4^{\bullet-}$, $O_2^{\bullet-}$, Fe(IV), and $^1O_2$ to degradation of TC, respectively.

The DMPOX adducts generation process caused by further radical-mediated oxidation of DMPO-OH (Equations S4-6).

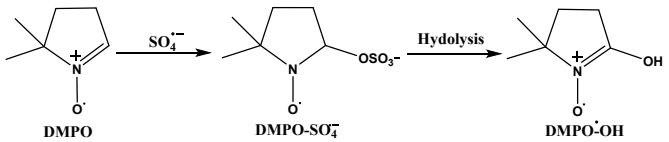

(4)

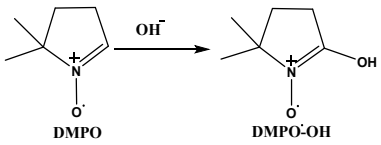

(5)

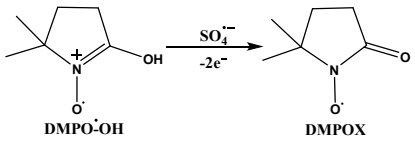

(6)

$^1O_2$ formation mechanism (Equations S7-9) :

$$HSO_5^- \rightarrow SO_5^{\cdot-} + H^+ + e^- \quad (7)$$

$$SO_5^{\cdot-} + SO_5^{\cdot-} \rightarrow S_2O_8^{2-} + {}^1O_2 \quad (8)$$

$$SO_5^{\cdot-} + SO_5^{\cdot-} \rightarrow 2\ SO_4^{2-} + {}^1O_2 \quad (9)$$

The susceptibilities (Equations S10) that originate from the magnetizations abide by the Curie-Weiss law (Equations S11), and the value of C can be calculated through the

linear fitting of χ^{-1}-T, where C is the Curie constant.The effective magnetic moment (μ_{eff}) can be calculated by Equations S12.

$$\chi=M/H \quad (10)$$

$$\chi=C/(T-\Theta) \quad (11)$$

$$\mu_{eff}=\sqrt{8C}\mu_B \quad (12)$$

Results and Discussion

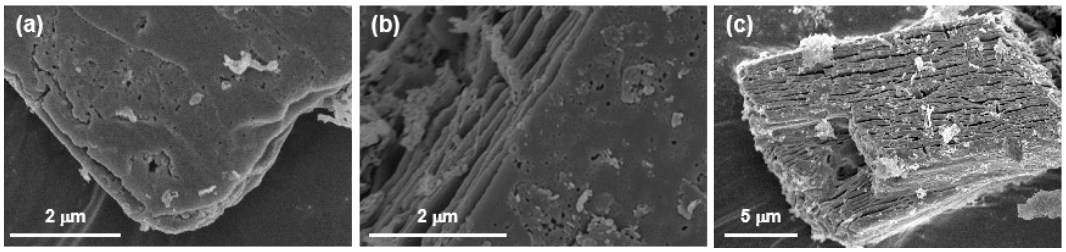

Figure S1. SEM images of (a) 2-Fe-CN, (b) 3-Fe-CN and (c) 4-Fe-CN.

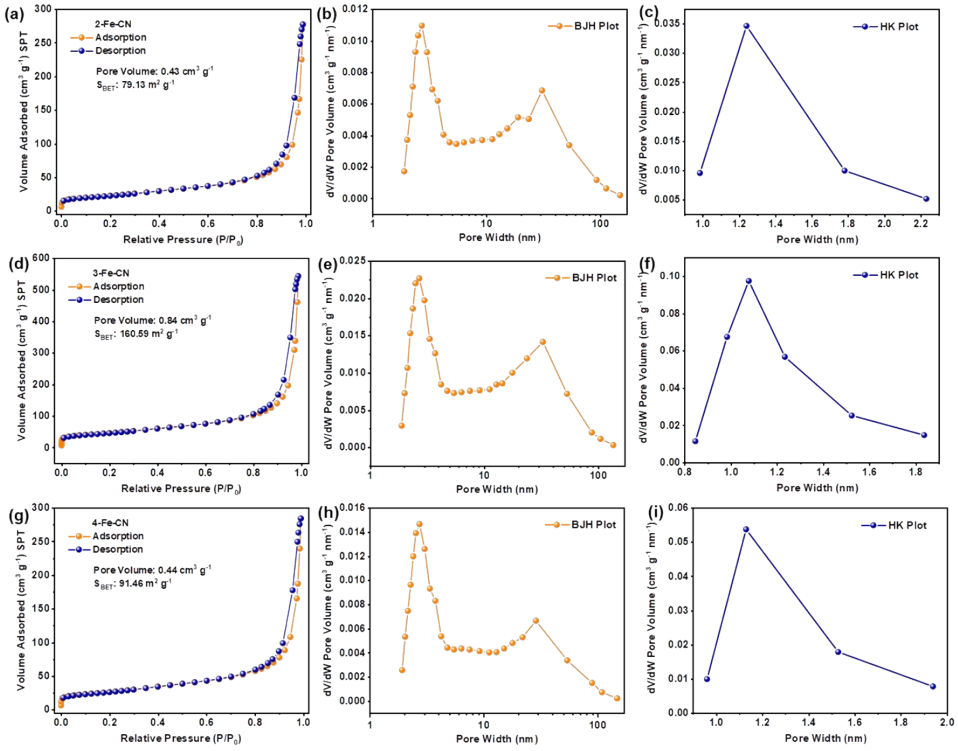

Figure S2. N_2 adsorption-desorption isotherms of (a) 2-Fe-CN, (d) 3-Fe-CN and (g) 4-Fe-CN. BJH plots of (b) 2-Fe-CN, (e) 3-Fe-CN and (h) 4-Fe-CN. HK plots of (c) 2-Fe-CN, (f) 3-Fe-CN and (i) 4-Fe-CN.

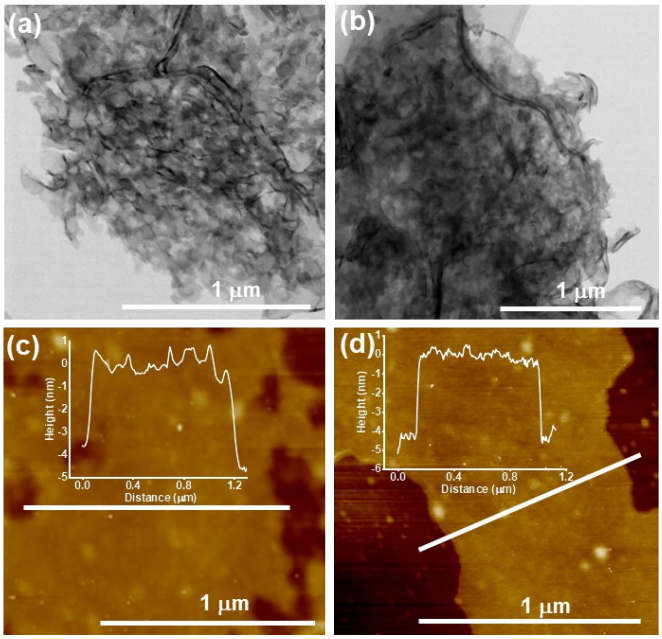

Figure S3. TEM images of (a) 2-Fe-CN and (b) 3-Fe-CN, AFM images of (c) 2-Fe-CN and (d) 3-Fe-CN.

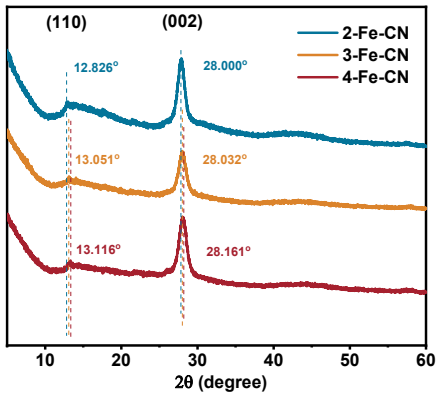

Figure S4. XRD pattern.

The two typical diffraction peaks located at 2θ = 12.826° - 13.116° and 28.000° - 28.161° were corresponded to the in-plane repeating units of tri-s-triazine and the graphite stacking of the polymer, respectively.

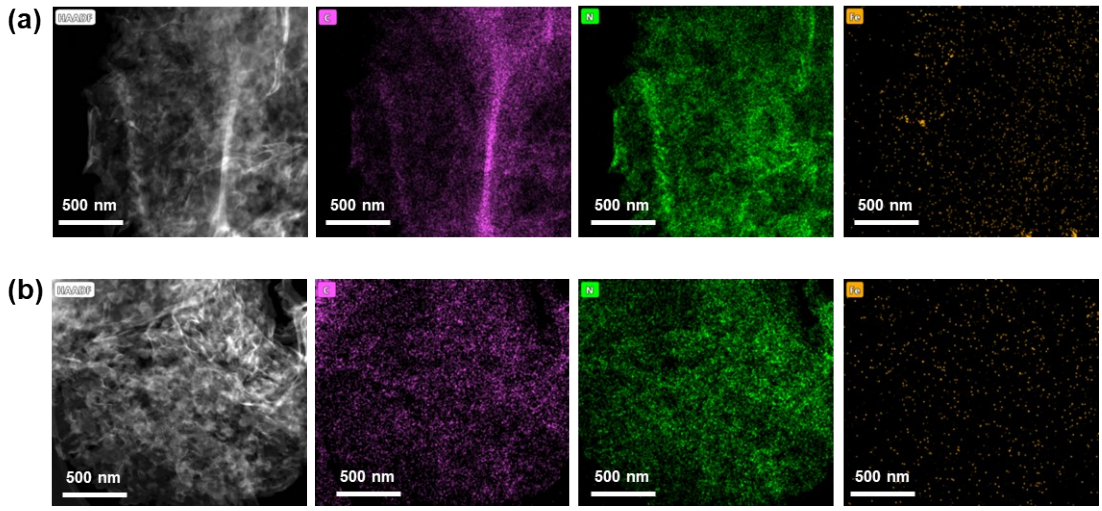

Figure S5. Energy-dispersive X-ray (EDX) elemental mapping of (a) 2-Fe-CN and (b) 3-Fe-CN.

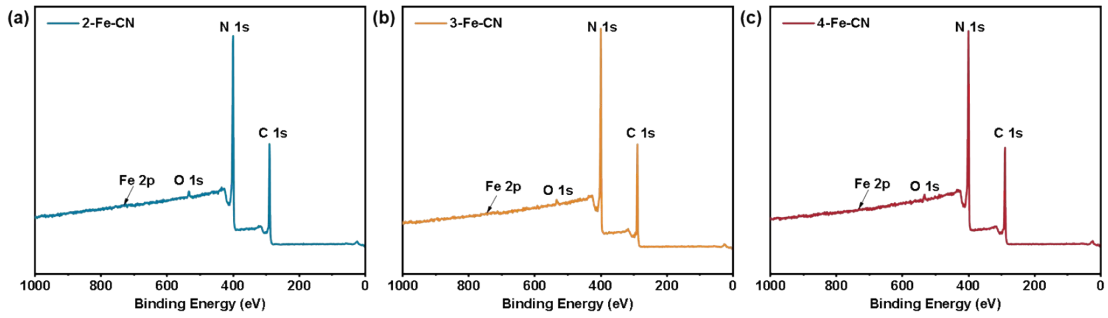

Figure S6. Full XPS survey of (a) 2-Fe-CN, (b) 3-Fe-CN, and (c) 4-Fe-CN.

As shown in Figure S6, the signals of C, N, O, and trace Fe were observed in the spectra survey of all the catalysts.

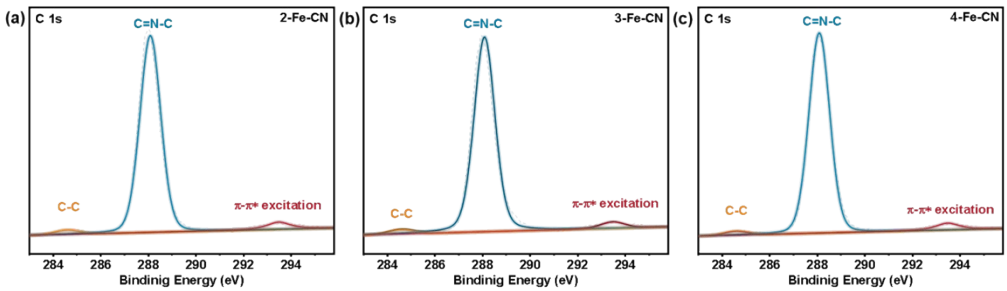

Figure S7. The high-resolution XPS spectra of C 1s for (a) 2-Fe-CN, (b) 3-Fe-CN and (c) 4-Fe-CN.

As shown in Figure S7, Fe atoms did not coordinate to C atoms, as evidenced by the similar C 1 s XPS spectra for 2-Fe-CN, 3-Fe-CN and 4-Fe-CN.

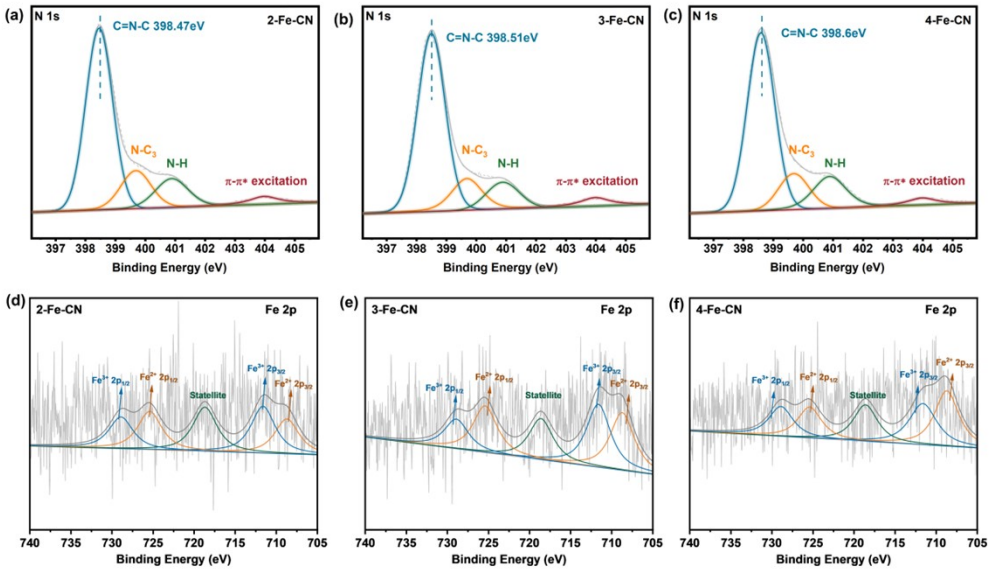

Figure S8. N 1 s XPS spectra of (a) 2-Fe-CN, (b) 3-Fe-CN and (c) 4-Fe-CN. Fe 2p XPS spectra of (d) 2-Fe-CN, (e) 3-Fe-CN and (f) 4-Fe-CN.

In N 1s region of Fe-CNs, the dominant nitrogen specie in all catalysts was the hybridized aromatic nitrogen atom (C=N-C), which is favorable for binding Fe atoms [21]. Moreover, the C=N-C peak of 4-Fe-CN shifted to higher binding energy compared with 2-Fe-CN and 3-Fe-CN, indicating that the chemical state of the N atom in the tri-s-triazine unit changed after changing heating rates. The Fe 2p XPS spectra exhibit a large number of miscellaneous peaks due the low Fe contents in the samples. All the Fe 2p spectra exhibit two Fe species, which were indexed to the ferric state of the Fe $2p_{3/2}$ and Fe $2p_{1/2}$.

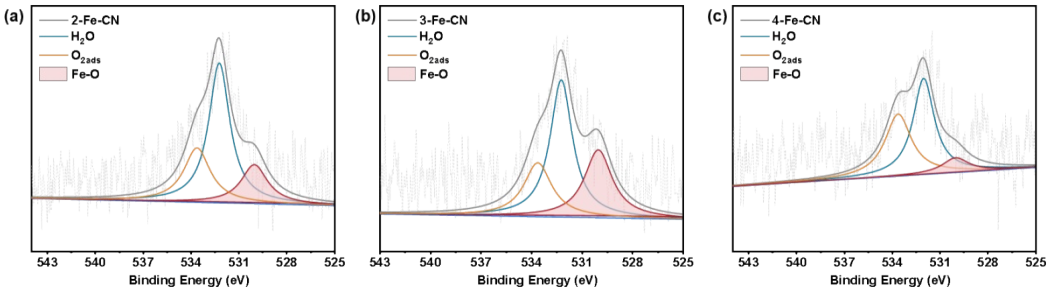

Figure S9. The high-resolution XPS spectra of O 1s for (a) 2-Fe-CN, (b) 3-Fe-CN and (c) 4-Fe-CN.

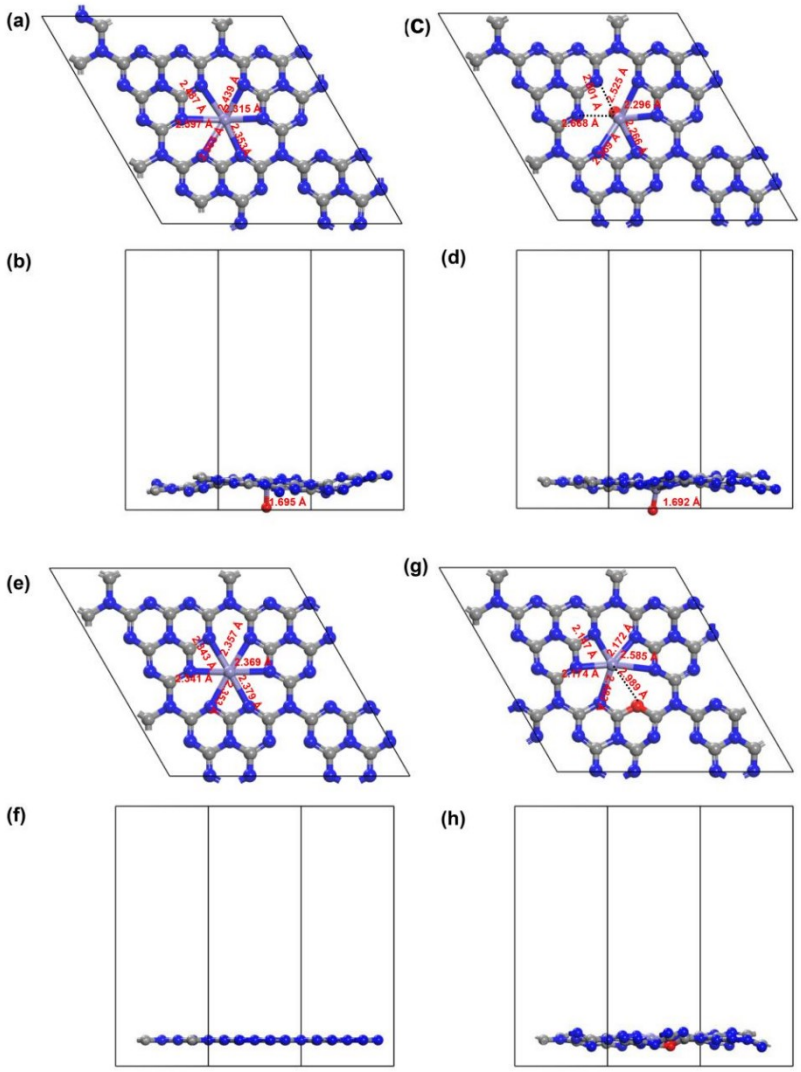

Figure S10. The corresponding structures and the C-N/C-O bond lengths of Fe-CNs calculated by DFT methods. (a)Top view and (b) front view of 2-Fe-CN ($FeON_6$) where the oxygen atom in the vertical direction. (c) Top view and (d) front view of 3-Fe-CN ($FeON_4$) where the oxygen atom in the vertical direction. (e)Top view and (f) front view of 4-Fe-CN (FeN_6). (g) Top view and (h) front view of 3-Fe-CN where the oxygen atom replaced one of six nitrogen atoms in the hole of C_3N_4 substrate.

As shown in the Figure S10a-f, the calculated Fe-N and Fe-O lengths of Fe-CNs are slightly longer than the experimental ones. We also considered that the oxygen atom replaced one of six nitrogen atoms in the hole of C_3N_4 substrate (Figure S10g-h) to simulate sample 3-Fe-CN. After optimization, the distance of Fe and O atoms was 2.989 Å, which was quite longer than the experimentally measured Fe-O length (1.53 Å), and this model was less stable than the model where the oxygen atom was perpendicular to the C_3N_4 substrate. Furthermore, as shown in Figure S4, the strongest XRD peak, which

is due to the stacking of the conjugated aromatic system [17, 18], gradually shifted to higher diffraction angle with increasing heating rate, corresponding to the gradually decreasing interlayer spacing (Table S2), which verified that the interlayer spacing of 2-Fe-CN and 3-Fe-CN were wider than that of 4-Fe-CN due to the vertically coordinated oxygen atoms. Therefore, the oxygen atoms of 2-Fe-CN and 3-Fe-CN preferred to bind Fe atom at the vertical direction of C_3N_4 surface.

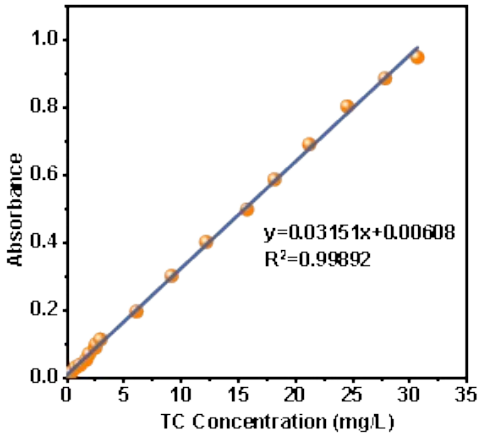

Figure S11. The UV standard curve of tetracycline.

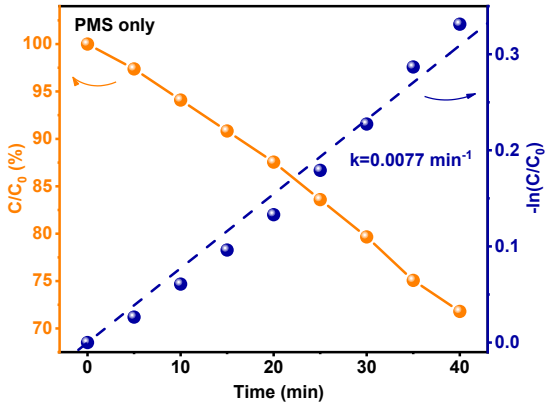

Figure S12. Degradation and first-order reaction kinetics of TC removal by activating PMS without catalyst. Conditions: $[PMS]_0$=1 mM, $[TC]_0$=5 mg L^{-1}, [Temp.] = 25±2 ° C, initial pH without adjustment.

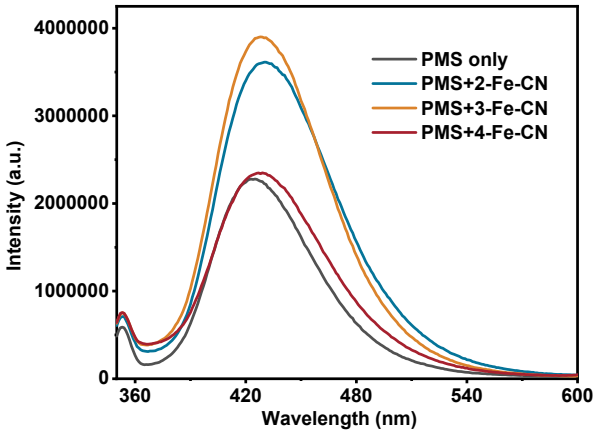

Figure S13. PL intensity of TA-OH in PMS only, 2-Fe-CN, 3-Fe-CN, and 4-Fe-CN activated PMS systems.

The qualitative analysis of •OH was used by the terephthalic acid photoluminescence (TA-PL) technique.[11] The PL intensity of 2-hydroxy terephthalic (TA-OH) at 425 nm (the probe for •OH) increased in 2-Fe-CN/PMS and 3-Fe-CN/PMS systems, but remained almost constant in 2-Fe-CN/PMS system, indicating a large amount of •OH was produced in the 2-Fe-CN/PMS and 3-Fe-CN/PMS systems, but not in the 4-Fe-CN/PMS system.

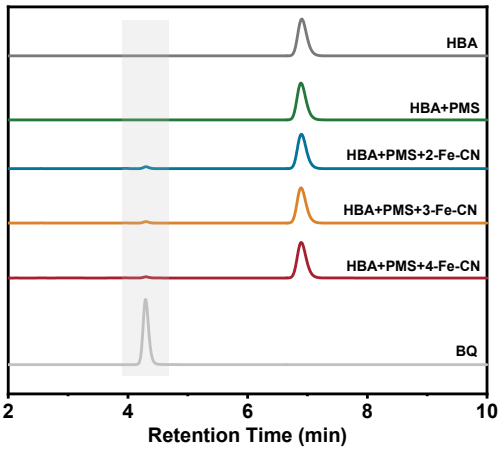

Figure S14. HPLC spectra of HBA in PMS only, 2-Fe-CN, 3-Fe-CN, and 4-Fe-CN activated PMS systems.

The quantitation of $SO_4^{\bullet-}$ was determined based on the indirect quantitation of BQ, which is the major degradation byproduct of HBA.[20] When HBA was used to probe for $SO_4^{\bullet-}$, weak singles corresponding to BQ were recorded at the retention time of 4.3 min during all the systems.

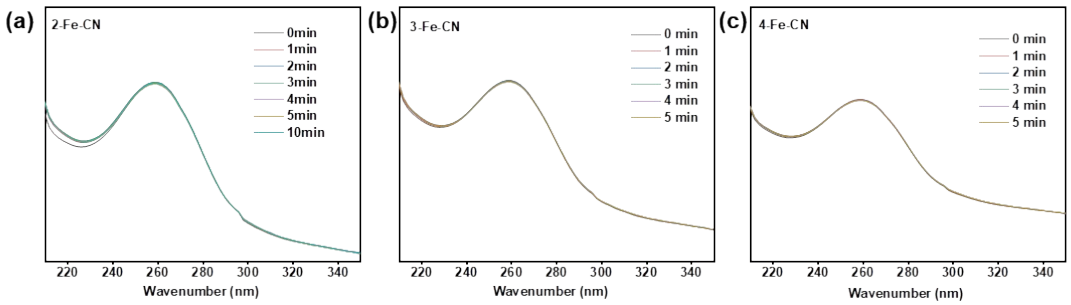

Figure S15. UV spectra of NBT in PMS only, 2-Fe-CN, 3-Fe-CN, and 4-Fe-CN activated PMS systems.

The production of $O_2^{\bullet-}$ was examined by the NBT method.[10]

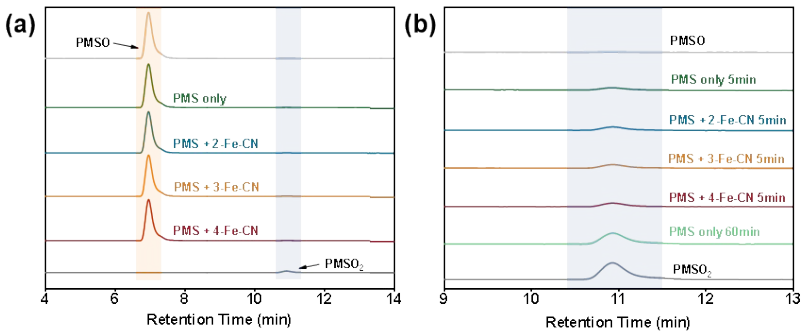

Figure S16. HPLC spectra of PMSO in PMS only, 2-Fe-CN, 3-Fe-CN, and 4-Fe-CN activated PMS systems.

The Fe(IV) was identified by $PMSO_2$ originate from Fe(IV)-derived PMSO.[11] When the PMSO was used to probe for high valent iron-oxo species, no obvious singles corresponding to methyl phenyl sulfone ($PMSO_2$) was recorded at the retention times of 10.9 min during the reaction (Figure S18a), and further calculation of the peak area ratio of PMSO in different systems showed no significant difference (Figure S18b, Table S3), implying the absence of high valent iron-oxo species.

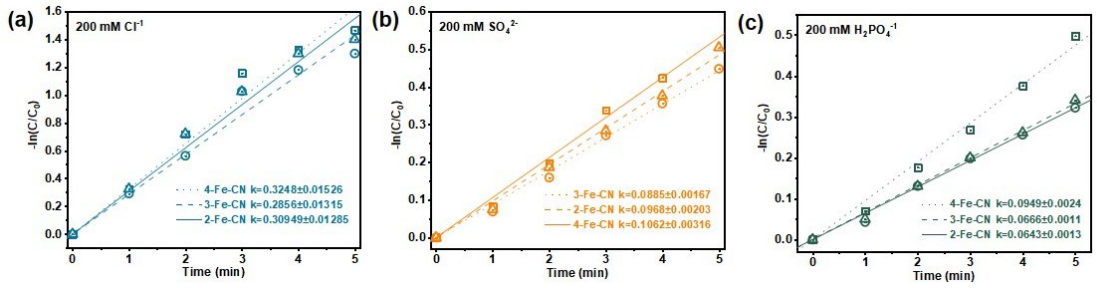

Figure S17. The first-order reaction kinetics of TC removal by activating PMS under (a) 200 mM Cl^-, (b) 200 mM SO_4^{2-} and (c) 200 mM $H_2PO_4^-$ with 4-Fe-CN.

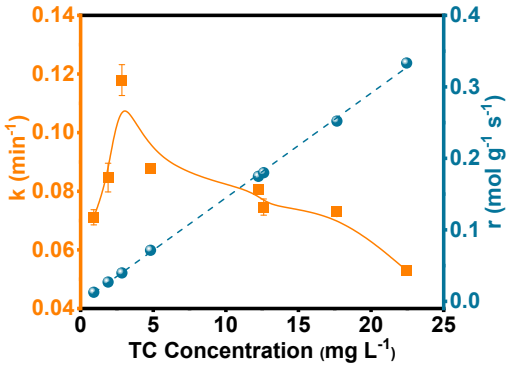

Figure S18. The reaction rate constant of the catalytic degradation and the rate of disappearance of TC under different TC concentration.

The catalytic activity of 4-Fe-CN was determined at different TC concentrations, from an environmentally relevant low concentration in lagoons or aquaculture (2 mg L^{-1}) to a median concentration value of industrial wastewaters (30 mg L^{-1}) [21], to determine the removal and rate of disappearance of TC degradation. The linear increasing trend in r suggested that the number of reaction sites at the catalyst surfaces was not a limiting factor of the catalytic reaction [23]. At low TC concentration, the TC concentration gradient between the catalyst surface and the solution is small, and the low mass transfer rate in batch mode made it difficult for pollutants to contact the catalyst surface, resulting in a lower catalytic degradation rate. An increase in the TC concentration resulted in a higher number of molecules available for degradation, resulting in a higher k value. Given the constant catalyst and PMS mass, the number of generated ROS was the same and hence the rise in reaction rate can only be attributed to the higher number of molecules present at the surface (first-order reaction rate) [23]. Above 4 mg L^{-1} concentration, the decrease of k value was observed, which may indicate that the catalyst surfaces become saturated with reactant TC molecules and hence the amount of absorbed PMS molecules limits TC removal.

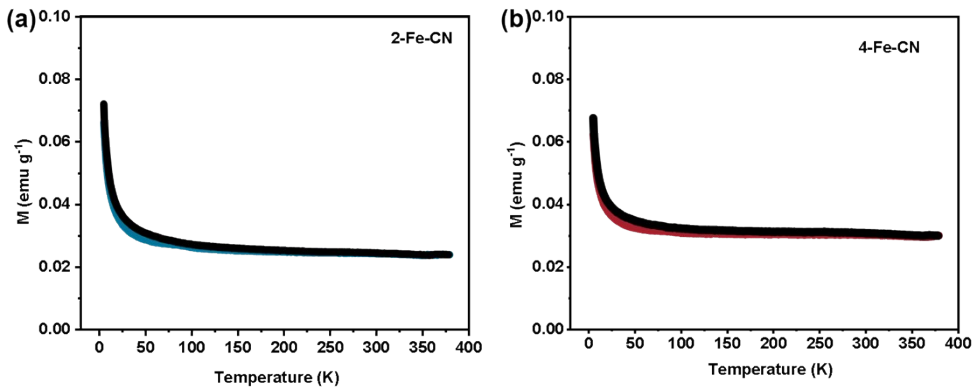

Figure S19. ZFC/FC curves over (a) 2-Fe-CN and (b) 4-Fe-CN measured at 1 kOe.

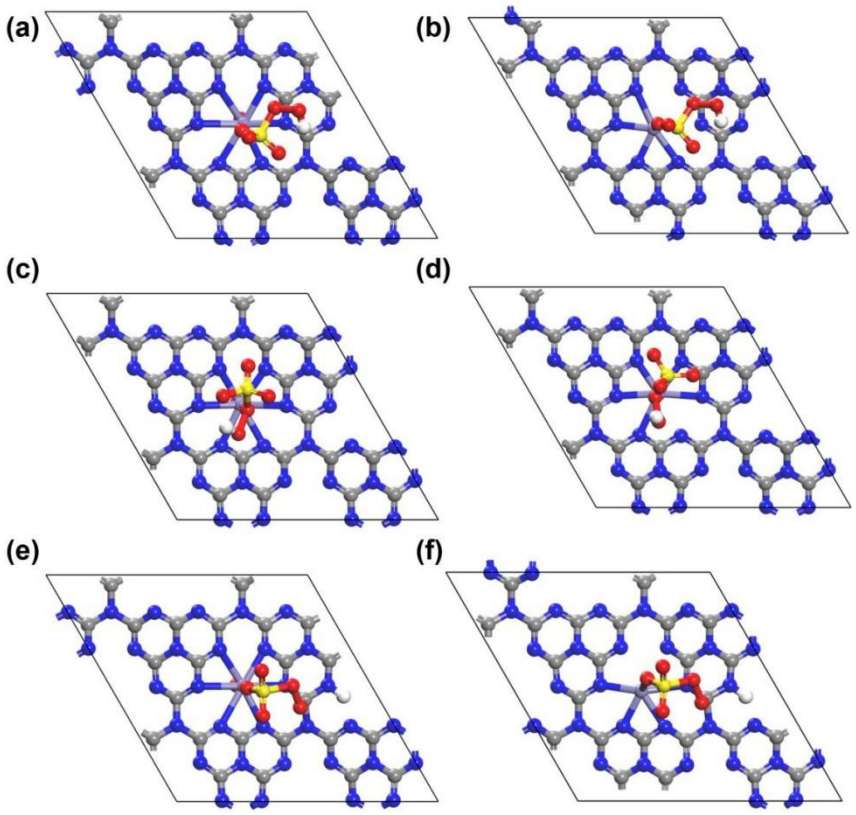

Figure S20. Optimized configurations of O1-site of PMS adsorbed on (a) 2-Fe-CN ($FeON_6$), and (b) 4-Fe-CN (FeN_6). Optimized configurations of O2-site of PMS adsorbed on (c) 2-Fe-CN ($FeON_6$), and (d) 4-Fe-CN (FeN_6). The dissociation of PMS on (e) 2-Fe-CN ($FeON_6$) and (f) 4-Fe-CN (FeN_6).

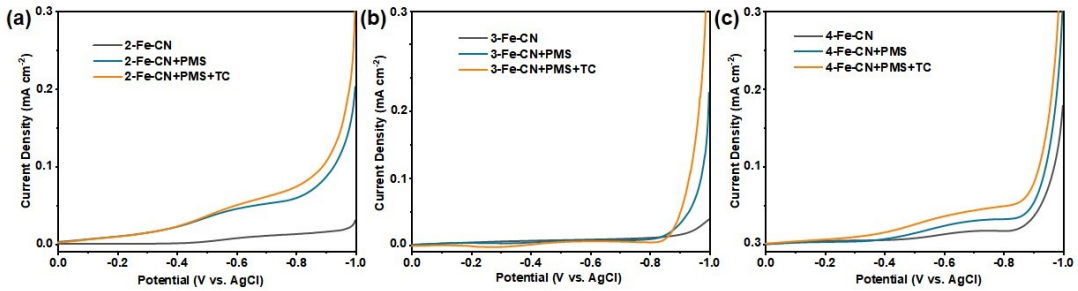

Figure S21. LSV curves of 2-Fe-CN ($FeON_6$), 3-Fe-CN ($FeON_4$) and 4-Fe-CN (FeN_6) under different conditions.

The electron-transfer process between pollutants, catalysts, and oxidants was intuitively examined by linear-sweep voltammetry (LSV) test. As shown in Figure S22, the current density of the Fe-CNs electrode significantly increased in the presence of PMS, which confirms that the reactive complexes were initially formed between PMS and Fe-CNs [22]. Besides, compared to 2-Fe-CN and 3-Fe-CN containing oxygen ligand on Fe atom, the higher current density of FeN6 after adding PMS indicated that it was easier to adsorb PMS and conduct electron transfer with PMS.

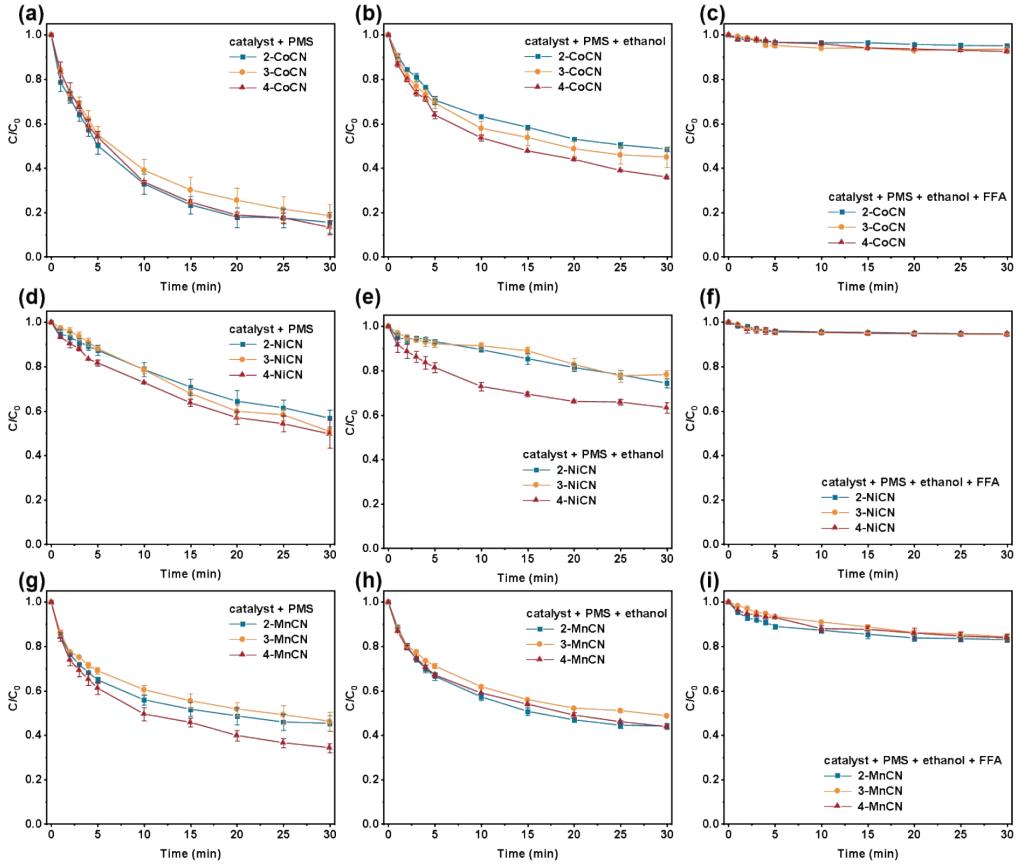

Figure S22. Degradation of TC by activating PMS in (a) x-CoCN/PMS system, (b) x-CoCN/PMS/ethanol system, (c) x-CoCN/PMS/ethanol/FFA system, (d) x-NiCN/PMS system, (e) x-NiCN/PMS/ethanol system, (f) x-NiCN/PMS/ethanol/FFA system, (g) x-MnCN/PMS system, (h) x-MnCN/PMS/ethanol system, and (i) x-MnCN/PMS/ethanol/FFA system. Conditions: [PMS]0 = 1mM, $[pollutants]_0$ = 10 mg L^{-1}, initial pH value, [ethanol]=500 mM, [FFA]=10 mM, 0.2 g L^{-1} of catalyst dosage .

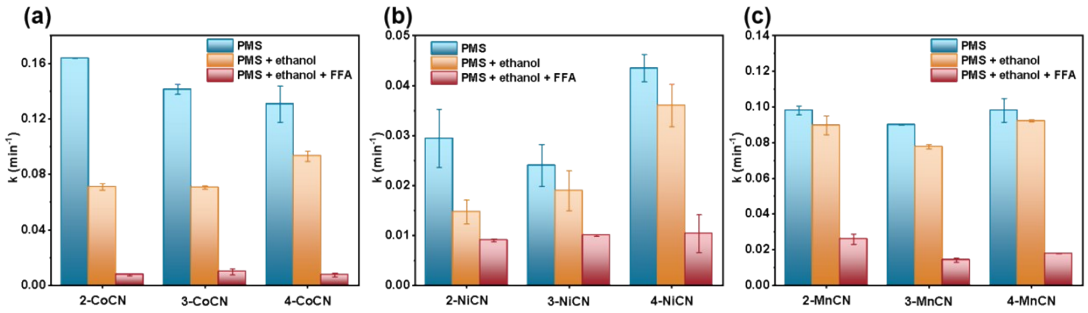

Figure S23. The k values of the (a) x-Co-CN, (b) x-Ni-CN, and (c) x-Mn-CN systems using ethanol (500 mM), and FFA (10 mM) as scavengers during quenching experiments.

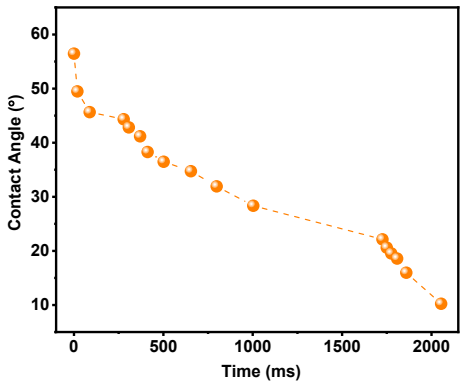

Figure S24. Dynamic water contact angle in the air of 4-Fe-CN-CM.

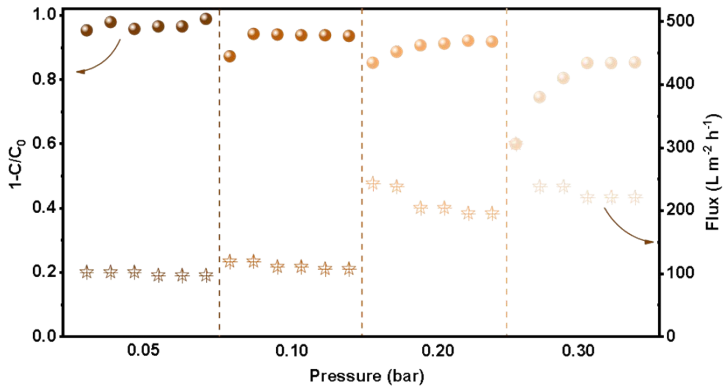

Figure S25. The TC degradation and flux of 4-Fe-CN-CM under different pressures.Conditions: $[PMS]_0$ = 1mM, $[pollutants]_0$ = 5 mg L^{-1}, initial pH value.

The dead-end filtration operating pressure was optimized in terms of balancing catalytic performance and water flux of 4-Fe-CN-CM. As shown in Figure S29, with

the increasing pressure, the membrane flux increased while the removal efficiency decreased, whereby the ~ 98% TC degradation was achieved at an ultra-low pressure 0.05 bar and permeance of ~ 101.9 L m^{-2} h^{-1}. The flux decay accelerated with increasing pressure but essentially without decay at 0.05 bar, which probably due to the tighter packing of the sheets under higher pressure.

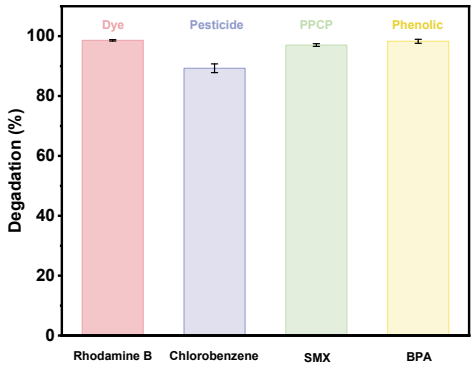

Figure S26. Some other pollutants degradation of 4-Fe-CN-CM. Conditions: $[PMS]_0$ = 1mM, $[pollutants]_0$ = 5 mg L^{-1}, pressure = 0.05 bar, initial pH value.

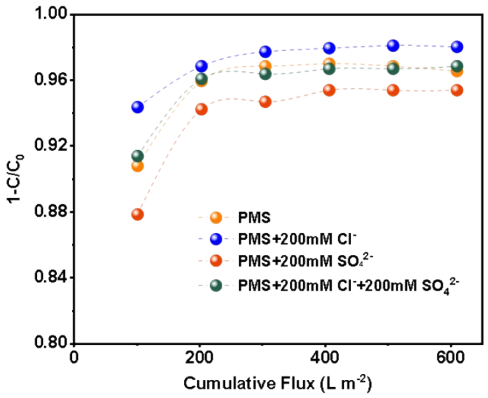

Figure S27. The TC degradation of 4-Fe-CN-CM under high-salinity environment. Conditions: $[PMS]_0$ = 1mM, $[TC]_0$ = 5 mg L^{-1}, pressure = 0.05 bar, initial pH value.

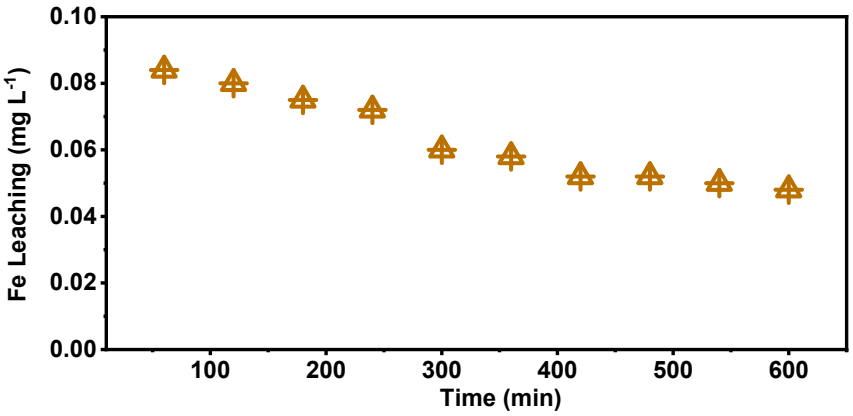

Figure S28. The Fe leaching of 4-Fe-CN-CM during long time operation.

Table S1. EXAFS fitting parameters at the Fe K-edge for various samples.

Sample	Path	N[a]	R(Å)[b]	σ^2(Å^2)[c]	ΔE_0(eV)[d]	R factor
Fe foil	Fe-Fe1	8.00	2.47	0.0049	6.25	0.0053
	Fe-Fe2	6.00	2.85	0.0057	6.25	
Fe_2O_3	Fe-O	5.90	2.01	0.0128	-1.45	0.0095
	Fe-Fe1	4.00	2.96	0.0041	-1.45	
	Fe-Fe2	1.00	3.46	0.0050	5.61	
FeO	Fe-O	6.00	2.11	0.0156	-2.00	0.0069
	Fe-Fe	12.20	3.07	0.0141	-2.00	
2-Fe-CN	Fe-N	5.81	2.13	0.0160	6.44	0.0164
	Fe-O	1.00	1.43	0.0160	-9.49	
3-Fe-CN	Fe-N	4.00	2.11	0.0099	7.85	0.0197
	Fe-O	1.07	1.53	0.0146	7.64	
4-Fe-CN	Fe-N	6.00	2.09	0.0179	4.38	0.0172

[a] CN, coordination number; [b] R, distance between absorber and backscatter atoms; [c] σ^2, Debye-Waller factor to account for both thermal and structural disorders; [d] ΔE_0, inner potential correction; R factor indicates the goodness of the fit. According to the experimental EXAFS fit of Fe foil by fixing CN as the known crystallographic value. Fitting range: $3.0 \leq k$ (/Å) ≤ 13.2 and $1.0 \leq R$ (Å) ≤ 2.9 (Fe foil); $2.7 \leq k$ (/Å) ≤ 10.4 and $1.0 \leq R$ (Å) ≤ 3.3 (Fe2O3); $3.0 \leq k$ (/Å) ≤ 12.8 and $1.0 \leq R$ (Å) ≤ 3.0 (FeO); $3.0 \leq k$ (/Å) ≤ 10.0 and $1.0 \leq R$ (Å) ≤ 2.3 (2-Fe-CN); $3.0 \leq k$ (/Å) ≤ 12.1 and $1.0 \leq R$ (Å) ≤ 2.8 (3-Fe-CN); $3.0 \leq k$ (/Å) ≤ 10.0 and $1.0 \leq R$ (Å) ≤ 2.5(4-Fe-CN).

Table S2. The (002) planes 2θ of 2-Fe-CN, 3-Fe-CN, and 4-Fe-CN in XRD pattern and the calculated d values.

catalyst	2θ (°)	d (nm)
2-Fe-CN	28.000	0.3184
3-Fe-CN	28.032	0.3181
4-Fe-CN	28.161	0.3166

Table S3. PMSO peak area ratio of different systems in HPLC spectra.

	PMSO peak area ratio (%)
PMS+PMSO	99.3
2-Fe-CN+PMS+PMSO	99.0
3-Fe-CN+PMS+PMSO	98.9
4-Fe-CN+PMS+PMSO	98.9

Table S4. Comparison of the first-order rate constant k values.

type	catalytic membrane	pollutants	retention time	removal rate (%)	k (min^{-1})
catalyst nanoparticles	Co–CN [24]	TC	3 min	100	0.19
	Co@rGO-N,S [25]	TC	20 min	98	0.23
	SA Fe-g-C_3N_4 [26]	TC	40 min	93	0.045
	CuHNPs-7.5 [27]	TC	30 min	100	0.12
	Fe_3O_4 [28]	TC	60 min	80	0.018
	SACoN/BCN [29]	sulfamethazine	40 min	79.1	0.0668
catalytic membranes	PVDF-CCNM [23]	TC	1.1 s	93.4	158.80
	Co_3O_4/C@SiO_2 catalysis membrane [30]	BPA	3.1 s	100	0.042
	PAN/LFC [31]	TC	15 min	> 99	0.25
	FeOCl-CM [32]	para-chlorobenzoic acid (pCBA)	8 s	85	13.20
	Fe_3O_4−CM [33]	pCBA	40 s	90	2.96
	4-Fe-CN-CM (this work)	TC	51.3 ms	96.5	4224

Table S5. Comparison of the reusability.

SACs	pollutants	oxidants	operation time	Pollutant removal efficiency
Co_{SA}-N_3C [34]	BPA / 50 μM	PDS / 2 mM	5 min of one cycle; run five cycles total 25 min	decreased from 100% to 80%
$Fe_xMo_{1-x}S_2$ [35]	Aniline / 10 μM	PMS / 1 mM	20 min of one cycle; run five cycles total 100 min	decreased from 100% to 50%
Mn–ISAs@CN[36]	BPA / 20 mg L^{-1}	PMS / 0.2 mg L^{-1}	10 min of one cycle; run five cycles total 50 min	decreased from 100% to 85%
Fe-g-C_3N_4[37]	M. aeruginosa	PDS / 1 mM	15 min of one cycle; run three cycles total 45 min	decreased from 96.3% to 9.1%
Fe@COF[38]	Orange II / 20 mg L^{-1}	PMS / 0.65 mM	45 min of one cycle; run four cycles total 180 min	decreased from 100% to 54%
DFeNC[39]	SMX / 5 mg L^{-1}	PDS / 1 mM	90 min of one cycle; run three cycles total 270 min	decreased from 100% to 45%
SA-Fe-NC[40]	BPA / 100 μM	PMS / 2 mM	3 min of one cycle; run five cycles total 15 min	decreased from 100% to 80%
ZIF-CoN_3P-C[41]	sulfadiazine / 10 mg L^{-1}	PMS / 1 mM	30 min of one cycle; run five cycles total 150 min	decreased from 100% to 80%
4-Fe-CN-CM (this work)	TC	PMS / 1 mM	continuous filtrate operation for 600 min	decreased from 96.5% to 93.8%

References

[1] L. Zhang, X. Jiang, Z. Zhong, L. Tian, Q. Sun, Y. Cui, X. Lu, J. Zou, S. Luo, Carbon nitride supported high-loading Fe single-atom catalyst for activation of peroxymonosulfate to generate $^1O_2$ with 100 % selectivity, Angew. Chem. Int. Ed. 60 (2021) 21751-21755.

[2] H. Funke, M. Chukalina, A. C. Scheinost, A new FEFF-based wavelet for EXAFS data analysis, J. Synchrotron Radiat. 14 (2007) 426-432.

[3] B. Ravel, M. Newville, ATHENA, ARTEMIS, HEPHAESTUS: data analysis for X-ray absorption spectroscopy using IFEFFIT, J. Synchrotron Radiat. 12 (2005) 537-541.

[4] H. Funke, M. Chukalina, A. Rossberg, Wavelet analysis of extended x-ray absorption fine structure data, Phys. Scr. 232 (2005) 115a00232.

[5] L. Zhang, Y. Zhang, J. Wei, W. Liu, Perovskite $LaFe_xCo_{1-x}O_{3-\lambda}$ deposited SiO_2 catalytic membrane for deeply cleaning wastewater, Chem. Eng. J. 403 (2021) 126386.

[6] C. Wang, J. Kim, M. Kim, H. Lim, M. Zhang, J. You, J.-H. Yun, Y. Bando, J. Li, Y. Yamauchi, Nanoarchitectured metal-organic framework-derived hollow carbon nanofiber filters for advanced oxidation processes, J. Mater. Chem. A 7 (2019) 13743-13750.

[7] L. Niu, G. Zhang, G. Xian, Z. Ren, T. Wei, Q. Li, Y. Zhang, Z. Zou, Tetracycline degradation by persulfate activated with magnetic γ-Fe_2O_3/CeO_2 catalyst: Performance, activation mechanism and degradation pathway, Sep. Purif. Technol. 259 (2021) 118156;

[8] S. Adhikari, H. Lee, D. Kim, Efficient visible-light induced electron-transfer in z-scheme MoO_3/Ag/C_3N_4 for excellent photocatalytic removal of antibiotics of both ofloxacin and tetracycline, Chem. Eng. J. 391 (2020) 123504.

[9] G. Kresse, J. Furthmüller, Efficient iterative schemes for ab initio total-energy calculations using a plane-wave basis set, Phys. Rev. B 54 (1996) 11169-11186.

[10] J. Perdew, K. Burke, M. Ernzerhof, Generalized gradient approximation made simple, Phys. Rev. Lett. 77 (1996) 3865-3868.

[11] P. Blöchl, Projector augmented-wave method, Phys. Rev. B 50 (1994) 17953-17979.

[12] S. Grimme, J. Antony, S. Ehrlich, H. Krieg, A consistent and accurate ab initio parametrization of density functional dispersion correction (DFT-D) for the 94 elements H-Pu, J. Chem. Phys. 132 (2010) 154104.
[13] C. Chu, J. Yang, X. Zhou, D. Huang, H. Qi, S. Weon, J. Li, M. Elimelech, A. Wang, J.-H. Kim, Cobalt single atoms on tetrapyridomacrocyclic support for efficient peroxymonosulfate activation, Environ. Sci. Technol. 55 (2020) 1242-1250.
[14] X. Jiang, Q. Xing, X. Luo, F. Li, J. Zou, S. Liu, X. Li, X. Wang, Simultaneous photoreduction of Uranium(VI) and photooxidation of Arsenic(III) in aqueous solution over g-C_3N_4/TiO_2 heterostructured catalysts under simulated sunlight irradiation, Appl. Catal. B Environ. 228 (2018) 29-38.
[15] Z. Wang, J. Jiang, S. Pang, Y. Zhou, C. Guan, Y. Gao, J. Li, Y. Yang, W. Qiu, C. Jiang, Is sulfate radical really generated from peroxydisulfate activated by Iron(II) for environmental decontamination? Environ. Sci. Technol. 52 (2018) 11276-11284.
[16] J. Li, S. Ghoshal, W. Liang, M.-T. Sougrati, F. Jaouen, B. Halevi, S. McKinney, G. McCool, C. Ma, X. Yuan, Structural and mechanistic basis for the high activity of Fe-N-C catalysts toward oxygen reduction, Energy Environ. Sci. 9 (2016) 2418-2432.
[17] X. Wang, K. Maeda, A. Thomas, K. TAkanabe, G. Xin, J. Carlsson, K. Domen, M. Antonietti, A metal-free polymeric photocatalyst for hydrogen production from water under visible light, Nat. Mater. 8 (2009) 76-80.
[18] H. Li, C. Shan, B. Cai, Fe(III)-doped g-C_3N_4 mediated peroxymonosulfate activation for selective degradation of phenolic compounds via high-valent Iron-oxo species, Environ. Sci. Technol. 52 (2018) 2197-2205.
[19] N. Jiang, H. Xu, L. Wang, J. Jiang, T. Zhang, Nonradical oxidation of pollutants with single-atom-Fe(III)-activated persulfate: Fe(V) being the possible intermediate oxidant, Environ. Sci. Technol. 54 (2020) 14057-14065.
[20] M. Xing, W. Xu, C. Dong, Y. Bai, J. Zeng, Y. Zhou, J. Zhang, Y. Yin, Metal sulfides as excellent Co-catalysts for H_2O_2 decomposition in advanced oxidation processes, Chem 4 (2018) 1359-1372.
[21] P. Segura, M. François, C. Gagnon, S. Sauvé, Environ. Review of the occurrence of anti-infectives in contaminated wastewaters and natural and drinking waters, Health Perspect. 117 (2009) 675-684.
[22] Z. Wang, W. Wang, W. Wang, Y. Yuan, Q. Wu, H. Hu, High-valent iron-oxo species mediated cyclic oxidation through single-atom triple bond Fe-N_6 sites with high peroxymonosulfate utilization rate, Appl. Catal. B Environ. 305 (2022) 121049.

[23] N. Lu, H. Lin, S. Xu, J. Wang, Q. Han, F. Liu, Bone/muscle-inspired polymer porous matrix toughened carbon nanofibrous catalytic membranes for robust emerging contaminants removal, Chem. Eng. J. 442 (2022) 136069.
[24] X. Zhang, B. Xu, S. Wang, X. Li, C. Wang, B. Liu, F. Han, Y. Xu, P. Yu, Y. Sun, Tetracycline degradation by peroxymonosulfate activated with CoNx active sites: Performance and activation mechanism, Chem. Eng. J. 431 (2022) 133477.
[25] X. Feng, Z. Xiao, H. Shi, B. Zhou, Y. Wang, H. Chi, X. Kou, N. Ren, How nitrogen and sulfur doping modified material structure, transformed oxidation pathways, and improved degradation performance in peroxymonosulfate activation, Environ. Sci. Technol. 56 (2022) 14048-14058.
[26] X. Peng, J. Wu, Z. Zhao, X. Wang, H. Dai, L. Xu, G. Xu, Y. Jian, F. Hu, Activation of peroxymonosulfate by single-atom Fe-g-C_3N_4 catalysts for high efficiency degradation of tetracycline via nonradical pathways: Role of high-valent iron-oxo species and Fe-N_x sites, Chem. Eng. J. 427 (2022) 130803.
[27] T. Guo, L. Jiang, H. Huang, Y. Li, X. Wu, Enhanced degradation of tetracycline in water over Cu-doped hematite nanoplates by peroxymonosulfate activation under visible light irradiation, J. Hazard. Mater. 416 (2021) 125838.
[28] S. She, J. Wang, J. Liu, C. Gao, Y. Li, L. Yang, X. Wu, S. Song, Reusing warm-paste waste as catalyst for peroxymonosulfate activation toward antibiotics degradation under high salinity condition: Performance and mechanism study, Chem. Eng. J. 426 (2021) 131295.
[29] X. Zhao, X. Jia, H. Li, H. Zhang, X. Zhou, Y. Zhou, H. Wang, L. Yin, T. Wågberg, G. Hu, Efficient degradation of health-threatening organic pollutants in water by atomically dispersed cobalt-activated peroxymonosulfate, Chem. Eng. J. 450 (2022) 138098.
[30] J. Xie, Z. Liao, M. Zhang, L. Ni, J. Qi, C. Wang, X. Sun, L. Wang, S. Wang, J. Li, Sequential Ultrafiltration-Catalysis Membrane for Excellent Removal of Multiple Pollutants in Water, Environ. Sci. Technol. 55 (2021) 2652-2661.
[31] L. Zhang, N. Yang, Y. Han, X. Wang, S. Liu, L. Zhang, Y. Sun, B. Jiang, Development of polyacrylonitrile/perovskite catalytic membrane with abundant channel-assisted reaction sites for organic pollutant removal, Chem. Eng. J. 437 (2022) 135163.
[32] S. Zhang, T. Hedtke, Q. Zhu, M. Sun, S. Weon, Y. Zhao, E. Stavitski, M. Elimelech, J.-H. Kim, Membrane-confined Iron oxychloride nanocatalysts for highly

efficient heterogeneous Fenton water treatment, Environ. Sci. Technol. 55 (2021) 9266-9275.
[33] S. Zhang, M. Sun, T. Hedtke, A. Deshmukh, X. Zhou, S. Weon, M. Elimelech, J.-H. Kim, Mechanism of heterogeneous Fenton reaction kinetics enhancement under nanoscale spatial confinement. Environ. Sci. Technol. 54 (2020) 10868-10875.
[34] X. Liang, D. Wang, Z. Zhao, T. Li, Z. Chen, Y. Gao, X. Hu, Engineering the low-coordinated single cobalt atom to boost persulfate activation for enhanced organic pollutant oxidation, Appl. Catal. B Environ. 303 (2022) 120877.
[35] L. Huang, C. Zhou, M. Shen, E. Gao, C. Zhang, X. Hu, Y. Chen, Y. Xue, Z. Liu, Persulfate activation by two-dimensional MoS2 confining single Fe atoms: performance, mechanism and DFT calculations, J. Hazard Mater. 389 (2020) 122137
[36] J. Yang, D. Zeng, Q. Zhang, R. Cui, M. Hassan, L. Dong, J. Li, Y. He, Single Mn atom anchored on N-doped porous carbon as highly efficient Fenton-like catalyst for the degradation of organic contaminants, Appl. Catal. B Environ. 279 (2020) 19363.
[37] H. Zhang, B. Yu, X. Li, Y. Li, Y. Zhong, J. Ding, Inactivation of Microcystis aeruginosa by peroxydisulfate activated with single-atomic iron catalysis: efficiency and mechanisms, J. Environ. Chem. Eng. 10 (2022) 108310.
[38] Y. Yao, H. Yin, M. Gao, Y. Hu, H. Hu, M. Yu, S. Wang, Electronic structure modulation of covalent organic frameworks by single-atom Fe doping for enhanced oxidation of aqueous contaminants, Chem. Eng. J. 209 (2019) 115211.
[39] Y. Shang, X. Liu, Y. Li, Y. Gao, B. Gao, X. Xu, Q. Yue, Boosting fenton-like reaction by reconstructed single Fe atom catalyst for oxidizing organics: synergistic effect of conjugated π-π sp_2 structured carbon and isolated Fe-N_4 sites, Chem. Eng. J. 446 (2022) 137120
[40] Y. Gao, Y. Zhu, T. Li, Z. Chen, Q. Jiang, Z. Zhao, X. Liang, C. Hu, Unraveling the high-activity origin of single-atom iron catalysts for organic pollutant oxidation via peroxymonosulfate activation, Environ. Sci. Technol. 55 (2021) 8318-8328.
[41] Y. Zou, J. Hu, B. Li, L. Lin, Y. Li, F. Liu, X. Li, Tailoring the coordination environment of cobalt in a single-atom catalyst through phosphorus doping for enhanced activation of peroxymonosulfate and thus efficient degradation of sulfadiazine, Appl. Catal. B Environ. 312 (2022) 121408.